














Quantifying the interplay between fine structure and geometry of an individual molecule on a surface

Manuel Steinbrecher ¹, Werner M. J. van Weerdenburg ¹, Etienne F. Walraven ¹, Niels P. E. van Mullekom ¹, Jan W. Gerritsen ¹, Fabian D. Natterer ², Danis I. Badrtidinov ^{3,1}, Alexander N. Rudenko ^{4,3,1}, Vladimir V. Mazurenko ³, Mikhail I. Katsnelson ^{1,3}, Ad van der Avoird ¹, Gerrit C. Groenenboom ¹ and Alexander A. Khajetoorians ^{1,*}

¹*Institute for Molecules and Materials, Radboud University, 6525 AJ Nijmegen, The Netherlands*

²*Department of Physics, University of Zürich, 8057 Zürich, Switzerland*

³*Theoretical Physics and Applied Mathematics Department, Ural Federal University, 620002 Ekaterinburg, Russia*

⁴*School of Physics and Technology, Wuhan University, Wuhan 430072, China*



(Received 12 August 2020; accepted 10 March 2021; published 7 April 2021)

The pathway toward the tailored synthesis of materials starts with precise characterization of the conformational properties and dynamics of individual molecules. Electron spin resonance (ESR)-based scanning tunneling microscopy can potentially address molecular structure with unprecedented resolution. Here, we determine the fine structure and geometry of an individual titanium-hydride molecule, utilizing a combination of a newly developed millikelvin ESR scanning tunneling microscope in a vector magnetic field and *ab initio* approaches. We demonstrate a strikingly large anisotropy of the g tensor, unusual for a spin doublet ground state, resulting from a nontrivial orbital angular momentum stemming from the molecular ground state. We quantify the relationship between the resultant fine structure, hindered rotational modes, and orbital excitations. Our model system provides avenues to determine the structure and dynamics of individual molecules.

DOI: [10.1103/PhysRevB.103.155405](https://doi.org/10.1103/PhysRevB.103.155405)

I. INTRODUCTION

Precisely determining the fine structure, dynamics, and geometry of an individual molecule, with submolecular resolution, is a grand challenge in numerous fields of nanoscience. Scanning probe microscopy (SPM) has emerged as a surface imaging approach capable of intramolecular resolution of individual molecules [1,2], quantifying conformational modifications like the static Jahn-Teller distortion [3], or light-assisted conformational changes [4]. Complementary to imaging, SPM-based inelastic excitation spectroscopy has been successfully applied to infer the various intramolecular vibrational [5], rotational [6,7], or hindered rotational modes [8]. However, these methods lack the precision to quantify the interplay between structure and molecular geometry like methods such as electron spin resonance (ESR) [9,10]. These methods are also not well suited for studying low-energy dynamics, such as the quantum zero-point motion of hydrogen and other light elements that are quenched by strong tip-sample interactions. Moreover, the resolution of traditional SPM, particularly scanning tunneling microscopy (STM), is limited by both convolution [1,11,12] and current preamplifier-related bandwidth issues that preclude insight into the structure and rotational dynamics of individual molecules.

Hybrid methods have recently emerged, combining the spatial resolution of STM with temporal resolution [13,14] driven by continuous wave excitation [15]. THz-based STM [16,17] has been used to excite and quantify the vibra-

tional motion of an individual phthalocyanine molecule with picosecond precision [18]. Likewise, electron paramagnetic or spin resonance (EPR/ESR) has been established [15,19,20], based on a combination of microwave excitation of the STM junction, with the detection of spin-polarized current [21] of individual atoms. This technique, referred to as ESR-STM, has been used to quantify magnetic interactions, hyperfine couplings, and the coherent dynamics of individual magnetic impurities with unprecedented resolution [22–24]. However, in the spirit of traditional EPR/ESR, ESR-STM has yet to be applied to infer the molecular structure and the related low-energy modes of an individual molecule.

Here, we quantify the fine structure of an individual titanium-hydride (TiH) molecule on the surface of magnesium oxide (MgO) and use this to determine the molecular geometry and low-energy excitations of TiH with picometer precision. Utilizing an ESR-STM to access previously unmeasured low-frequency bands in multidirectional magnetic fields at millikelvin temperature, we observe a giant anisotropy in the g tensor concomitant with a spin- $\frac{1}{2}$ (doublet) ground state. Along a field direction parallel to the surface, the g factor nearly has the free electron value, as expected for an ideal doublet. However, the g factor is strongly renormalized in a field direction perpendicular to the surface, which has thus far not been measured. In light of the inability of conventional density functional theory (DFT), as well as the mean-field DFT + U approach to describe these experimental results, we adapted an approach based on quantum chemistry (QC) and exact quantum dynamics to properly account for the correlations in this molecular system. Using this approach, we include the Coulomb interactions generated by the ions of the surface and illustrate how the spin quartet electronic ground

*Corresponding author: a.khajetoorians@science.ru.nl

state of the isolated TiH molecule transforms into a doublet state as it approaches the MgO surface. We reveal that the origin of the strongly anisotropic g tensor stems from a sizeable orbital angular momentum of the electronic ground state, which DFT-based methods fail to predict, when the molecule is near the surface. Moreover, we quantify the g tensor in embedded cluster calculations, which yield good agreement with the experiments and enable determination of the structure and low-energy excitations of the molecule.

II. RESULTS

A. Electronic ground state calculation

TiH is a molecular radical relevant in molecular astrophysics and astrochemistry due to its abundance in space [25]. It has been predicted to host an electronic $^4\Phi$ ground state [25] with three parallel unpaired electrons and orbital occupation $[\text{Ar}]4\sigma^2(4\sigma^*)^13d_{x^2-y^2/xy}^13d_{xz/yz}^1$, where 4σ denotes the bonding molecular orbital formed between Ti and H and $4\sigma^*$ its antibonding counterpart. Nevertheless, there is no experimental data identifying its electronic structure in the gas phase. Starting from *ab initio* QC, we consider the TiH molecule in the gas phase with $C_{\infty v}$ symmetry to fully account for the orbital angular momentum. In the absence of the surface, TiH indeed resides in the $^4\Phi$ state, with a projected orbital angular momentum $\Lambda = 3$ and spin angular momentum (S) in a quartet configuration, $S = \frac{3}{2}$. In the gas phase, the $^4\Phi$ state is favored (green) over the excited $^2\Delta$ state (orange), with $\Lambda = 2$ and a doublet $S = \frac{1}{2}$, with an energy separation of 343 meV [Fig. 1(a)]. The $^2\Delta$ state contains a single unpaired electron with orbital occupation of $[\text{Ar}]4\sigma^2(4\sigma^*)^23d_{x^2-y^2/xy}^1$.

Magnetic atoms and molecules on surfaces are most often treated within DFT, where the effects of electron correlations are commonly considered in mean field approaches, such as DFT + U and dynamical mean-field theory (DMFT) [26,27]. By contrast, QC approaches can more precisely capture the electron correlations but are not often used in combination with surfaces due to the computational complexity introduced by the distance-dependent coupling with the band structure of the surface. Due to the ionic and insulating nature of MgO (band gap ≈ 6 eV) [28,29], we consider the surface with a point charge model where all charges are highly localized. This is a first approximation to the surface, and later, we discuss higher-level theory where the surface is more properly treated in an embedded cluster approach. We also utilized DFT + U (see Supplemental Material [30]), but this approach leads to an inaccurate prediction of the splitting of the doublet state and to a trivial value of the orbital angular momentum. In the QC approach, we accounted for the Mg and O atoms directly below TiH and mimic the rest of the surface by a finite lattice of point charges, $\pm 2e$, having the fourfold rotational symmetry of MgO(100), and used the lattice parameters obtained from the relaxed DFT + U calculations (see Sec. S8 in the Supplemental Material [30]).

The adsorption of TiH onto MgO strongly modifies the electronic structure of the molecule and limits its angular motion due to the ionic environment. Starting from gas-phase calculations, we computed the state energies of the $^4\Phi$ and $^2\Delta$ electronic states of the TiH molecule as a function of distance

(d) normal to the MgO surface [Fig. 1(a)]. We considered TiH adsorption on top of oxygen (top site) to directly compare with the experimental data. As the molecule approaches the surface, there is a crossover in the favored ground state from the $^4\Phi$ state to the $^2\Delta$ state, $d \leq 2.7$ Å. At the relaxed height from DFT + U (dashed line) at $d \approx 2.50$ Å [22,31], the $^2\Delta$ state is therefore the ground state. We later confirm the favorability of the $^2\Delta$ state, at the relaxed height from theory, with embedded cluster calculations. The change in the ground state can be attributed to a higher electron density below the TiH in the $^4\Phi$ state than in the $^2\Delta$ state, resulting in a larger repulsion from the underlying MgO unit with the $^4\Phi$ state than the $^2\Delta$ state. This also forces the H atom to reside above the Ti atom, while the latter is closer to the O site. For $d = 2.42$ Å, the degeneracy between the two preferred orbitals $^2\Delta_{x^2-y^2}$ (orange) and $^2\Delta_{xy}$ (cyan) is broken. This leads to a partially quenched orbital moment at short distances to the surface, which will be discussed later together with the precise values of the splitting and g tensor. The striking difference between QC and DFT + U [22,31] is that the molecule retains a sizeable orbital angular momentum compared with the negligible values resulting from DFT + U (see Table S2 in the Supplemental Material [30]). Additionally, DFT + U overestimates the splitting of the ground state by roughly a factor of five. Although the $^2\Delta$ ground state maintains a nontrivial orbital angular momentum, it hosts a spin doublet and should not be susceptible to residual magnetic anisotropy, in line with previous experimental observations [24].

B. ESR-STM of an individual TiH molecule

To probe the orbital angular momentum of the TiH molecule and the possible effect of a crystal field, we adopt ESR-STM [15] down to millikelvin temperatures [32,33] in magnetic field orientations parallel and perpendicular to the surface to extract the g tensor, as schematically depicted in Fig. 1(b). By operating at lower temperature, we access new frequency bands corresponding to absolute energies roughly an order of magnitude lower than previously studied [15]. Our use of magnetically stable bulk Cr probes [19,34] with additionally picked up Fe atoms ensures spin polarization at zero field and enables ESR-STM at both magnetic field polarities. After cold deposition of Ti, TiH molecules appeared on both top and bridge sites of a 2 monolayer (ML) thick patch of MgO grown on a Ag(100) surface (see Appendix A). We additionally codeposited Fe atoms on the surface for tip preparation and calibration, and both species can be identified by a combination of their apparent height [Fig. 1(c)] and spectroscopic fingerprints (see Sec. S1 in the Supplemental Material [30]). For the ESR measurements, we operated in two complementary modes, namely external magnetic field (B) sweep (B -sweep) mode or frequency (f) sweep (f -sweep) mode. In the first mode (B -sweep), we measured at selected values f , while the external field B_{ext} was swept, and in the second mode (f -sweep), B_{ext} was kept constant, while f was swept (see Appendix A).

We observed resonant excitations in both previously probed frequency bands as well as new band regimes (0.3–21 GHz). We note that the out-of-plane excitations have not

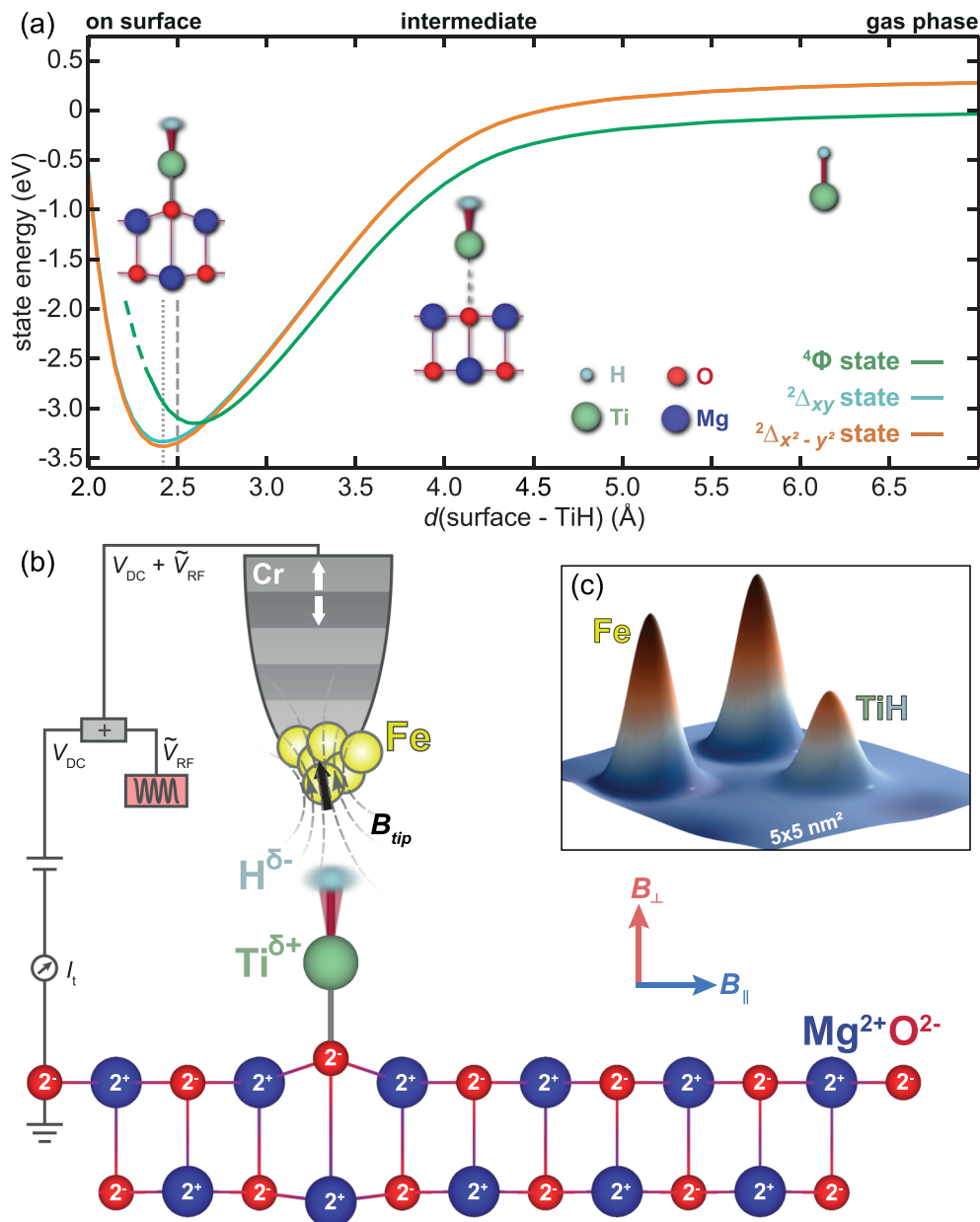


FIG. 1. Structure of the TiH molecule and influence of the surface. (a) Evolution of the $^2\Delta$ and $^4\Phi$ states of the TiH molecule as a function of distance from the surface of MgO, obtained from *ab initio* quantum chemistry (QC) calculations. The electronic ground state of the system changes from the $^4\Phi$ to the $^2\Delta$ state for the adsorbed TiH. The dashed line indicates the relaxed height obtained from DFT + U and the dotted line the energy minimum of the states from QC calculations. (b) Illustration of the TiH molecule adsorbed on the oxygen site of an ionic $Mg^{2+}O^{2-}$ surface. The \tilde{V}_{RF} is applied on the magnetic Cr tip and is added to V_{DC} as schematically sketched. (c) Three-dimensional representation of a constant-current scanning tunneling microscopy (STM) image of a TiH molecule adsorbed next to two Fe atoms. Different apparent heights for Fe (151 ± 8 pm) and TiH (103 ± 8 pm) clearly distinguish both adsorbate types ($V_{DC} = 30$ mV, $I_t = 10$ pA).

been previously studied in detail. The resonance peak shifts at rates that depend on the orientations of B_{ext} (Fig. 2). Measurements in B -sweep mode for B_{ext} in the \perp (red) and \parallel (blue) directions to the surface are shown in Fig. 2(b), measured at constant radiofrequency (RF) amplitude ($V_{RF} = 7.9$ mV) and at selected frequencies ranging from 1.165 to 10.92 GHz. Resonance peaks are each fitted with a Lorentzian (not shown), enabling precise identification of the peak location and width.

Strikingly, these linear trends have distinct slopes depending on the orientation of B_{ext} . The description of these

different slopes resides in the anisotropy of the g tensor, which is schematically depicted in Fig. 2(a). The allowed $\Delta\Omega = \pm 1$ (with $\Omega = \Lambda + \Sigma$, see definitions in Subsec. E) ESR transitions at a given frequency occur for different amplitudes of B_{ext} , depending on the magnetic field orientation. Likewise, the linear behavior was observed in both orientations for both polarities of B_{ext} , enabling the determination of the offset magnetic fields due to the magnetic probe. We performed f -sweep mode measurements on the same molecule in the band $f = [7.9\text{--}8.5 \text{ GHz}]$. Like the B -sweep mode, the peak

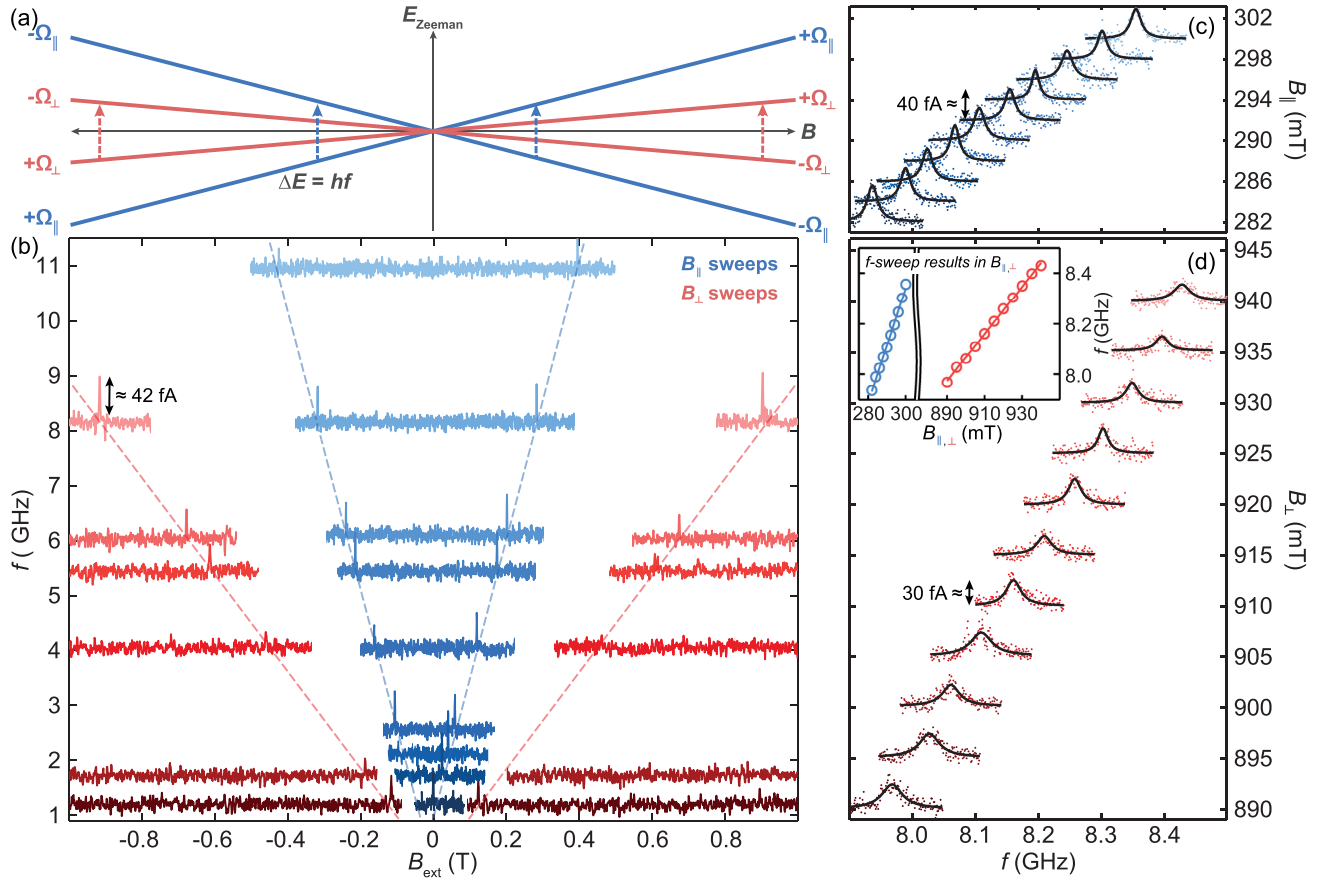


FIG. 2. Millikelvin electron spin resonance (ESR) scanning tunneling microscopy (STM) of a TiH molecule in variable field orientations. (a) Sketch of the Zeeman diagram for the level splitting of the doublet state in different field orientations B_{\parallel} (blue) and B_{\perp} (red). Dashed arrows of the same lengths indicate the allowed $\Delta\Omega = \pm 1$ transitions for a specific f (with $\Omega = \Lambda + \Sigma$). (b) B -sweep mode ESR measurements with the same microtip for two TiH molecules with the magnetic field swept in $\pm B_{\parallel}$ (blue) or $\pm B_{\perp}$ (red) direction. Peak positions are extracted from Lorentzian fits and subsequently fitted with a linear model (dashed lines). For the same selected frequencies, they appear at very different magnetic fields for the two directions, revealing an anisotropic g tensor with $g_{\parallel} = 1.80 \pm 0.02$ ($[25.2 \pm 0.2]$ GHz/T) and $g_{\perp} = 0.63 \pm 0.01$ ($[8.8 \pm 0.1]$ GHz/T) ($V_{DC} = 50$ mV, $I_t = 2$ pA, $f_{\text{chop}} = 877$ Hz, $V_{RF} = 7.9$ mV). f -sweep mode ESR measurements in (c) B_{\parallel} and (d) B_{\perp} direction with the same microtip and on the same TiH molecule as in the B_{\parallel} -sweep in (b). Solid lines represent Lorentzian fits to the experimental data. Linear fits to the extracted peak positions [inset in (d)] reveal $g_{\parallel} = 1.62 \pm 0.06$ ($[22.7 \pm 0.9]$ GHz/T) and $g_{\perp} = 0.66 \pm 0.02$ ($[9.3 \pm 0.3]$ GHz/T) ($V_{DC} = 50$ mV, $I_t = 2$ pA, $f_{\text{chop}} = 877$ Hz, $V_{RF} = 8.0$ mV).

positions extracted from Lorentzian fitting (solid lines) revealed an identical linear trend with slopes depending on the orientation of B_{ext} . Additional raw datasets of such experiments are presented in Sec. S3 and Figs. S7–S9 in the Supplemental Material [30].

C. Anisotropic g tensor

To ascertain the g tensor, as well as set an upper bound of a potential zero-field splitting, we performed repeated measurements in both modes, in bands from 382 MHz to 22 GHz. Figure 3(a) shows the extracted resonance peak positions of 21 experimental datasets with both measurement modes. All data points were recorded with the same measurement parameters for distinct microtips, different TiH molecules, as well as for various frequencies or B -field ranges and orientations. Both the B and f dependencies remain linear down to frequencies of 382 MHz and up to ≈ 21 GHz (inset). We note that we have not observed the hyperfine splitting on

the oxygen binding site as reported in Ref. [23]. We did observe nonlinear trends for some but not all datasets at low frequencies [Figs. 3(a) and S10 in the Supplemental Material [30]] that we attributed to a significant stray field of the STM tip B_{tip} with a component oriented orthogonal to the applied field B_{ext} (see Sec. S5 in the Supplemental Material [30]). To extract values of the slopes, all datasets were fitted individually with linear functions, excluding the nonlinear data (see Sec. S4 in the Supplemental Material [30]). A g factor was then extracted from each dataset assuming a fixed magnetic moment of $1 \mu_B$. All individually extracted g factors are plotted in Fig. 3(b). The error bars represent the standard deviation from the cumulative error of the slope from linear regression. The weighted means were calculated from all data points and reveal $g_{\parallel} = 1.67 \pm 0.16$ and $g_{\perp} = 0.61 \pm 0.09$. Here, the error corresponds to twice the weighted standard deviation. The weighted average of these values represents the extracted g factor for each distinct direction (\parallel and \perp). In this comprehensive analysis, we also included 10

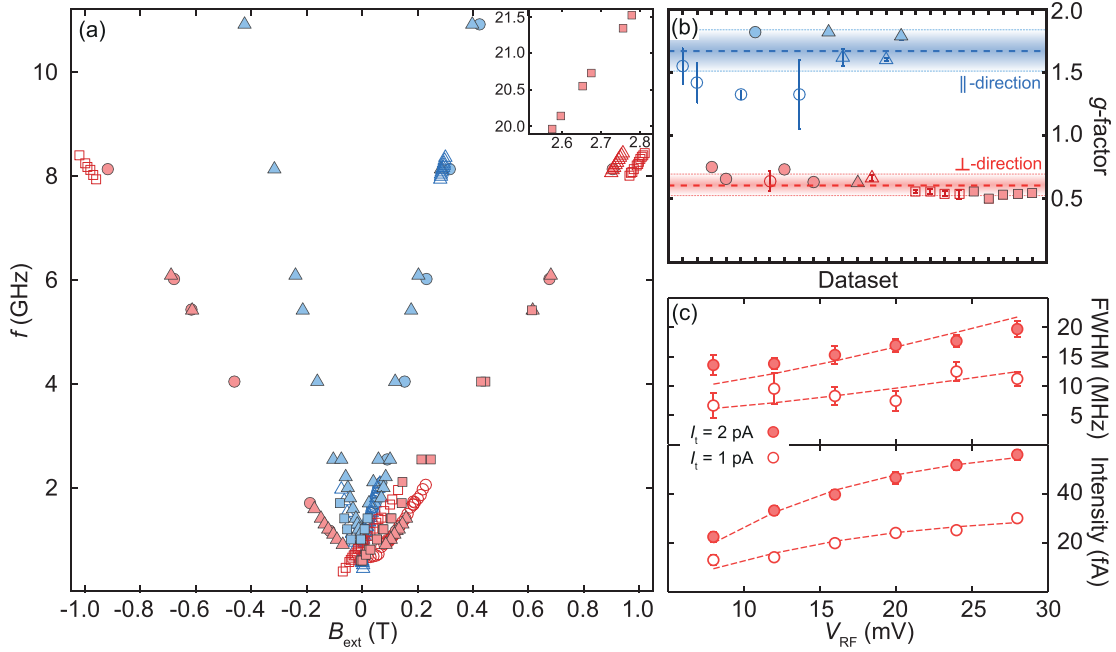


FIG. 3. Giant g -tensor anisotropy of TiH. (a) Extracted electron spin resonance (ESR) peak positions from 21 datasets on different molecules (indicated by different symbols) measured in two B -field directions \perp (red) or \parallel (blue). Filled or open symbols correspond to B - or f -sweep mode, respectively. Measurement parameters throughout all experiments were the same ($V_{\text{DC}} = 50$ mV, $I_t = 2$ pA, $V_{\text{RF}} = 8$ mV), except for the inset [$V_{\text{DC}} = 50$ mV, $I_t = 10$ pA, $\tilde{V}_{\text{RF}} = 4.466$ V (uncalibrated V_{RF})]. (b) Experimental g factors obtained from linear fits to the data in (a) as well as additionally included datasets with varied experimental parameters and tips (see Fig. S7 in the Supplemental Material [30] for a plot of all data). From 30 datasets in total, we obtain $g_{\parallel} = 1.67 \pm 0.16$ ($[23.4 \pm 2.29]$ GHz/T) and $g_{\perp} = 0.61 \pm 0.09$ ($[8.49 \pm 1.19]$ GHz/T). (c) Plots of the full width at half maximum (FWHM) (top) and ESR peak intensity (bottom) from V_{RF} power-dependent measurements of a TiH molecule extracted from fitting Fano lineshapes to the experimental data. Dashed lines indicate simultaneous fits within the 1 and 2 pA datasets, respectively, and reveal an asymptotic trend for the FWHM with V_{RF} .

additional datasets taken with different stabilization parameters and V_{RF} , which are shown in Fig. S10 in the Supplemental Material [30]. The error bars, which are often smaller than the symbol size, emphasize the high precision of the ESR-STM method [22], where g was determined with an error as small as $\Delta g = 0.0011$. Therefore, we can conclude that the scatter in the values of g stems from a physical mechanism and not from the precision of the measurement (see Sec. S9.5 in the Supplemental Material [30]).

We note that there are several mechanisms that lead to a variation in the reported g tensor. In addition to systematic variations resulting from the measurements, we observe a variation in the g tensor based on the given tip as well as for a given molecule. Not all molecules were measured in both measurement modes, nor were all molecules measured in both field directions with the same tip, leading to an apparent difference in the g -factor value in the y direction for the two different modes. We observe no variation in the precision between the two measurement modes in the z direction, where more statistics were measured.

The strong g -tensor anisotropy can result from a variety of phenomena. We can rule out the presence of a Jahn-Teller distortion, which would be accompanied by a crystal field splitting that is absent down to 382 MHz. This corresponds to an upper bound for a possible zero-field splitting of only $1.58 \mu\text{eV}$, an energy precision inaccessible by other methods like inelastic scanning tunnelling spectroscopy (ISTS). Complementary ISTS experiments without applied V_{RF} and

a non-spin-polarized tip confirmed the measured g -tensor anisotropy seen in ESR ($g_{\parallel, \text{ISTS}} = 1.84 \pm 0.01$; $g_{\perp, \text{ISTS}} = 0.50 \pm 0.01$; Fig. S14 in the Supplemental Material [30]). As we also illustrate later, TiH experiences a strong potential barrier with nearly cylindrical symmetry, which rules out a multiwell potential and a dynamic Jahn-Teller description. Due to the lower temperature of our present setup, compared with previous studies [22,24], the spin- $\frac{1}{2}$ ground state may enter a Kondo screening regime below a critical temperature. However, the magnetization of a spin- $\frac{1}{2}$ Kondo impurity exhibits a nonlinearity at energy scales below or near T_{K} [35], and we observe strictly linear behavior up to 21 GHz. These trends, including the g -tensor anisotropy, persist at elevated temperature up to 1.1 K (see Sec. S6 in the Supplemental Material [30]). Likewise, we observe no signature of a Kondo resonance in STS (Fig. S3 in the Supplemental Material [30]). Therefore, we conclude that the g -tensor anisotropy concomitant with the lack of any nonlinear trend or zero-field splitting is a direct result of the $^2\Delta$ molecular ground state, demonstrating the sizable orbital angular momentum of the molecule.

D. Linewidth analysis

In addition to the anisotropic g tensor of the molecule, we also observe a finite linewidth of a given resonance with an intrinsic linewidth comparable with that measured up to 50 times higher in temperature [19,22,24,36,37]. In Fig. 3(c), we illustrate the power dependence of one TiH molecule measured in f -sweep mode for different currents. We measured

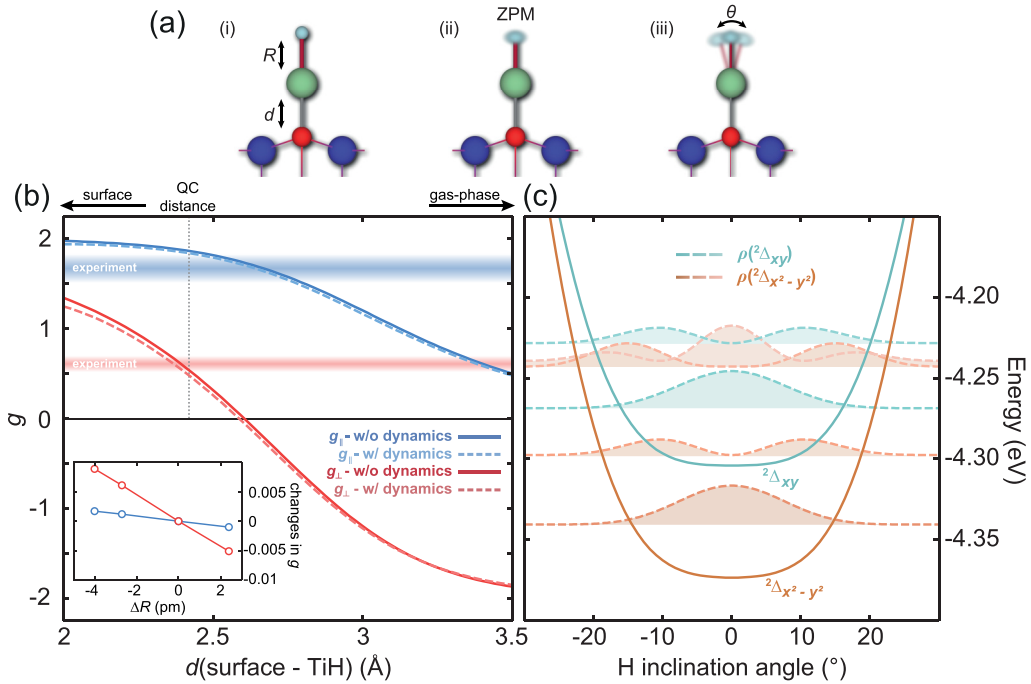


FIG. 4. Modeling the g tensor, the molecular geometry, and the hindered rotations. (a) Illustrations indicating the structural degrees of freedom of the TiH molecule: (i) bonding distance between Ti and O (d) or Ti and H (R), (ii) zero-point motion of H, and (iii) excited rotational mode. (b) Calculated in-plane (blue) and out-of-plane (red) g factors of the TiH without (solid lines) or with (dashed lines) rotational dynamics. The g tensor is highly sensitive to the adsorption height of the molecule. At $d = 2.42$ Å, the minimum found in quantum chemistry (QC) calculations [Fig. 1(a)], the experimentally observed anisotropic g tensor can very well be reproduced. The inset shows the small variations in g for changes of R . (c) Calculated potential wells (solid lines) for both ${}^2\Delta$ orbital states and densities ρ (dashed lines) of the wave functions for the corresponding equidistant energy levels as a function of inclination angle θ . Both are reminiscent of an anharmonic two-dimensional quantum oscillator, where an amplitude of $\approx 15^\circ$ can be deduced for the zero-point motion of the hydrogen.

and subsequently fitted the extracted widths (top graph) and the intensities (bottom graph) of the resonance peaks for V_{RF} ranging from 8 to 28 mV, like the reports in Refs. [22,36]. We observed an asymptotic trend toward a resonance linewidth of ≈ 6 MHz for $I_t = 1$ pA, which compares with the ≈ 3.5 MHz reported for the same settings at higher temperature [22]. The resonance linewidth is broadened, e.g., by scattering with electrons, variations in magnetic field or V_{RF} , and variations of the Rabi frequency caused by mechanical motion of the tip relative to the sample [24,38]. It has been shown that the linewidth can be strongly increased with increasing applied power [38,39]. Our experimental findings indicate that the likely broadening mechanisms are temperature independent in the measured temperature range. This rules out other temperature-dependent broadening mechanisms such as substrate electron scattering and spin-orbit coupling. It also suggests that the hyperfine coupling from the hydrogen nuclear moment or another degree of freedom may play a role in determining the saturated linewidth for the molecule.

E. Theoretical model of the structure and excitations

Having established that the electronic state of the TiH molecule on the surface has ${}^2\Delta$ symmetry, we present the model used to calculate the g tensor. We first discuss the free molecule, then introduce the effect of the crystal surface assuming the TiH molecule is vertical on the surface, and finally consider the effect of angular motion of the

molecule [Fig. 4(a)] on the g factors. We present results for a simple point-charge model of the surface, as well as embedded-cluster calculations on the complete-active-space multiconfigurational self-consistent-field (CASSCF) level and the internally contracted multireference configuration interaction (MRCI) level, which we did with the Molpro QC code [40].

For the free molecule, the spin $S = \frac{1}{2}$ Hund's case (a) wave functions are $|\Lambda, \Sigma\rangle$, where $\Lambda = \pm 2$ and $\Sigma = \pm \frac{1}{2}$ are the orbital and spin angular momentum projection quantum numbers. The spin-orbit coupling for these wave functions is given by $A_{\text{SO}}\Lambda\Sigma$, and since the spin-orbit coupling constant A_{SO} is positive, Λ and Σ have opposite signs in the lower fine-structure state, and $\Omega = \Lambda + \Sigma = \pm \frac{3}{2}$, while the upper state has $\Omega = \pm \frac{5}{2}$. In the field-free case, the states $|\Lambda, \Sigma\rangle$ and $|-\Lambda, -\Sigma\rangle$ are degenerate. Since spin-orbit coupling as well as the potential that describes the interaction with the surface commute with the time-reversal operator, it is convenient to use a time-reversal symmetry adapted basis

$$\Psi_{\pm}(\Lambda, \Sigma) = \frac{1}{\sqrt{2}}\{|\Lambda, \Sigma\rangle \pm |-\Lambda, -\Sigma\rangle\}. \quad (1)$$

The two-dimensional basis $\{\Psi_+(2, -1/2), \Psi_-(2, -1/2)\}$ describes the doubly degenerate lower fine-structure state. The degeneracy is lifted by the interaction with the magnetic field, which is described by the Zeeman Hamiltonian in atomic units

$$\hat{H}_{\text{Zeeman}} = \mu_{\text{B}}(\hat{\mathbf{L}} + g_e\hat{\mathbf{S}}) \cdot \mathbf{B}, \quad (2)$$

where \hat{L} and \hat{S} are the orbital and spin angular momentum vector operators, $g_e \approx 2.0023$ is the electron spin g factor, μ_B is the Bohr magneton ($\mu_B = \frac{1}{2}$ in atomic units), and \mathbf{B} is the magnetic field. A g factor is related to the derivative of the energy splitting with respect to the strength of the magnetic field $B \equiv |\mathbf{B}|$, and must be divided by μ_B . When the field is perpendicular to the surface, the degeneracy is lifted by the z components of the angular momentum operators, which couple the two basis functions, and we find, for $\Lambda = 2$ and $\Sigma = -\frac{1}{2}$,

$$g_{\perp} = 2|\langle \Psi_{-}(\Lambda, \Sigma) | \hat{L}_z + g_e \hat{S}_z | \Psi_{+}(\Lambda, \Sigma) \rangle| \quad (3)$$

$$= 2(\Lambda + g_e \Sigma) = 4 - g_e \approx 2. \quad (4)$$

When the field is parallel to the surface, the \hat{S}_x operator in the Zeeman Hamiltonian couples the lower and upper fine-structure states

$$\hat{S}_x \Psi_{\pm}(\Lambda, \Sigma) = \pm \frac{1}{2} \Psi_{\pm}(\Lambda, -\Sigma), \quad (5)$$

but this coupling is second order, and because it is the same for both time-reversal symmetries, the field does not lift the degeneracy of the lower state, and so $g_{\parallel} = 0$. However, there will be first-order coupling when we consider the fine-structure states mixed by the crystal field.

The effect of the crystal potential \hat{V}_S is to break the ($C_{\infty v}$) cylinder symmetry of the TiH molecule and lift the degeneracy of the $\Delta_{x^2-y^2}$ and Δ_{xy} components of the ${}^2\Delta$ state. With the TiH molecule vertically on top of an O ion, the system has fourfold symmetry, but we will use the Abelian symmetry group C_{2v} , for which the $\Delta_{x^2-y^2}$ and Δ_{xy} states are of A_1 and A_2 symmetry, respectively. The energies of the states are given by

$$V_1 = \langle \Delta_{x^2-y^2} | \hat{V}_S | \Delta_{x^2-y^2} \rangle, \quad (6)$$

$$V_2 = \langle \Delta_{xy} | \hat{V}_S | \Delta_{xy} \rangle, \quad (7)$$

and the off-diagonal element is zero by symmetry. The \hat{L}_z orbital angular momentum eigenstates are related to the real functions through

$$|\Lambda = \pm 2\rangle = \frac{1}{\sqrt{2}}(\Delta_{x^2-y^2} \pm i\Delta_{xy}), \quad (8)$$

so we find that the crystal field quenches the orbital angular momentum by coupling the $\Lambda = 2$ and $\Lambda = -2$ states,

$$\langle \Lambda = \pm 2 | \hat{V}_S | \Lambda = \mp 2 \rangle = \frac{V_1 - V_2}{2} \equiv \frac{V_c}{2}. \quad (9)$$

Just like the spin-orbit coupling, the crystal field cannot couple states with different time-reversal symmetry

$$\langle \Psi_{+}(\Lambda_1, \Sigma_1) | \hat{V}_S | \Psi_{-}(\Lambda_2, \Sigma_2) \rangle = 0, \quad (10)$$

but it will couple the fine-structure states with $\Omega = \frac{3}{2}$ and $\Omega = \frac{5}{2}$,

$$\left\langle \Psi_{\pm} \left(2, -\frac{1}{2} \right) \middle| \hat{V}_S \middle| \Psi_{\pm} \left(2, \frac{1}{2} \right) \right\rangle = \pm \frac{V_c}{2}. \quad (11)$$

Thus, in the presence of both spin-orbit coupling and the crystal field, the wave functions are found variationally by diagonalizing a 2×2 Hamiltonian matrix

$$\mathbf{H}_{\pm} = \begin{pmatrix} -A_{SO} & \pm \frac{V_c}{2} \\ \pm \frac{V_c}{2} & A_{SO} \end{pmatrix}. \quad (12)$$

The ground state is still doubly degenerate, and the g factors are found in closed form by computing how the magnetic field lifts this degeneracy, as for the free molecule. The eigenvectors of the Hamiltonian matrix only depend on the ratio of the diagonal and off-diagonal elements

$$r \equiv \left| \frac{V_c}{2A_{SO}} \right|, \quad (13)$$

and so the g factors are functions of the ratio r . In the Supplemental Material (Sec. S9.3) [30], we show that

$$g_{\parallel} = g_e \frac{r}{\sqrt{1+r^2}}, \quad (14)$$

$$g_{\perp} = \left| g_e - \frac{4}{\sqrt{1+r^2}} \right|. \quad (15)$$

Both the crystal field coupling V_c and the spin-orbit coupling depend on the height of the TiH above the surface. While the spin-orbit coupling varies only slightly from the gas phase to the equilibrium height, the crystal-field splitting obviously starts at zero in the gas phase, but increases exponentially near the surface [41]. As a result, not only the coupling which arises from the breaking of the cylinder symmetry must be known, but also the forces that determine the height of the molecule above the surface must be computed.

1. Electrostatic approximation

We first consider a point charge model for the crystal-field splitting. In Fig. 4(b), we show how g_{\parallel} and g_{\perp} depend on the height above the surface. For g_{\perp} , we left out the absolute value from Eq. (15) so it is easier to distinguish the strong coupling regime where $r > 1$ and the weak coupling where $r < 1$. In the figure, the dashed line indicates the height above the surface as calculated at the DFT + U level, and we see that the g factors at that distance are in good agreement with experiment.

We computed the electrostatic crystal field splitting in an MRCI calculation where we included a $21 \times 21 \times 2$ grid of point charges to represent the crystal. In these calculations, we also included the O ion right below the TiH and the Mg ion in the second layer of the crystal below the central O ion to account for the Pauli repulsion. These results are well converged with respect to the number of point charges. The adsorption height at this level of theory is 2.42 Å, close to the DFT + U value. Furthermore, we found that, if we set the point charges to (+1.7, -1.7) rather than the formal (+2, -2), the crystal field is reduced, but at the same time the adsorption height becomes smaller, and the effect on the g tensor is small (see Sec. S9.5.6 in the Supplemental Material [30]).

In our model, both g_{\parallel} and g_{\perp} are determined by a single parameter, the interaction ratio r [Eq. (13)]. In Fig. 5, we show the curve of possible combinations of g_{\parallel} and g_{\perp} within

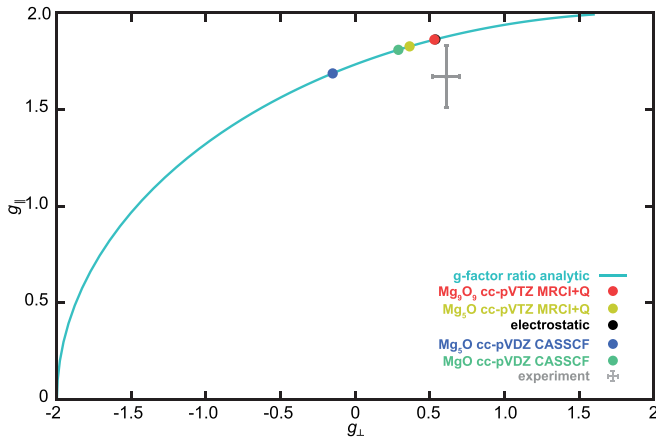


FIG. 5. Relation between g_{\parallel} and g_{\perp} for the ${}^2\Delta$ state. The curve represents the one-dimensional space in the theoretical model, parametrized by the ratio between the energy splitting and spin-orbit coupling. Results from the electrostatic model and embedded cluster calculations are represented by dots, together with experimental results given in gray with error bars. We note that the black and red dots nearly overlap.

this model. This figure also shows the experimental values for the g tensor and the error bars, which are near the curve of possible model results.

2. Second-order effects

It is straightforward to extend the model to include other low-lying states such as the ${}^2\Pi$ and ${}^4\Phi$ states. These states are coupled to the ${}^2\Delta$ state through spin-orbit coupling, giving rise to second-order spin-orbit effects. This introduces the energy separation and the spin-orbit coupling between the states as extra parameters, so Eqs. (14) and (15) no longer hold and so the results are no longer restricted to the curve in Fig. 5. However, since these low-lying states are not well described by single excitations of the ${}^2\Delta$ state, the couplings are most likely smaller than the coupling within the states. Some crude estimates suggest that the second-order spin-orbit

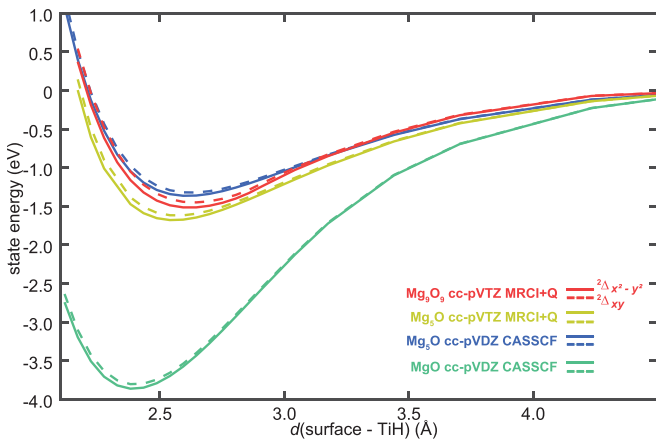


FIG. 6. Potential energy curves of the ${}^2\Delta$ state as a function of the height above the surface in various embedded cluster calculations.

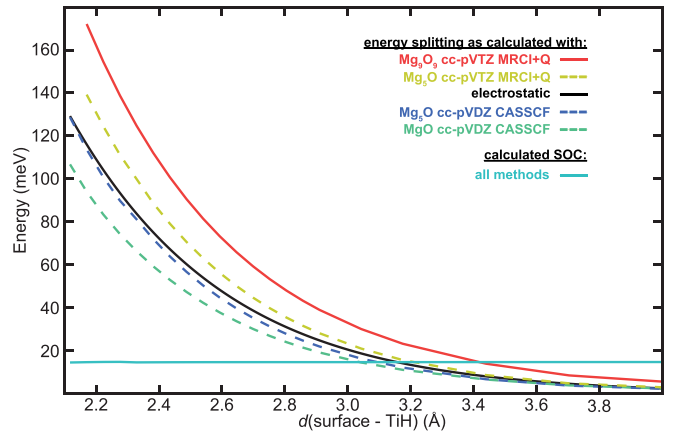


FIG. 7. Energy splitting and spin-orbit coupling constant of the ${}^2\Delta$ state as a function of the height above the surface in various embedded cluster calculations.

effects are very small, so we do not consider them further. In principle, the crystal field can couple the ${}^2\Delta$ state to neighboring doublet states, but because of the fourfold symmetry, coupling between $\Lambda = 2$ and $\Lambda = 1$ or 3 only occurs in high order, so we also ignore these second-order effects.

3. Embedded cluster calculations

To investigate the effect of going beyond the point-charge model for the crystal field splitting and the adsorption height, we performed a series of embedded cluster calculations, with four different clusters, up to Mg_9O_9 , a $3 \times 3 \times 2$ cluster of ions. In these calculations, point charges were added again to extend the clusters to $21 \times 21 \times 2$. Convergence with respect to the one-electron basis set and with respect to the treatment of electron correlation was studied. Details of these calculations and their results are given in Appendix B, Figs. 6–8 and Table I. The conclusion is that increasing the size of the cluster, using a larger one-electron basis, and treating the electron correlation at a higher level, all tend to get the result closer

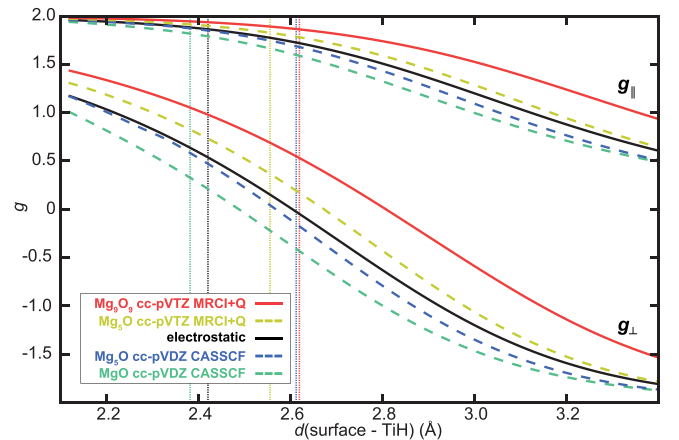


FIG. 8. g factors of the ${}^2\Delta$ state as a function of the height above the surface in the electrostatic model and using various embedded cluster calculations. Dotted vertical lines denote the optimal height above the surface in that method.

TABLE I. Convergence of embedded cluster calculations of g factors of TiH on MgO. Here, d denotes the height of the molecule above the surface, D_e the dissociation energy, and V_c the energy splitting of the ${}^2\Delta$ states. $A_{\text{SO}} = 110.05 \text{ cm}^{-1}$ was used here. The experimental values are $g_{\parallel} = 1.67 \pm 0.16$ and $g_{\perp} = 0.61 \pm 0.09$.

Cluster	cc-pVDZ		cc-pVTZ	
	CASSCF	CASSCF	MRCI	MRCI + Q
MgO				
d (Å)	2.39	2.40	2.37	2.36
D_e (eV)	-3.99	-3.16	-3.72	-3.84
V_c (cm^{-1})	464.41	470.85	565.47	602.48
g_{\parallel}	1.81	1.81	1.87	1.88
g_{\perp}	0.29	0.31	0.55	0.63
Mg₅O				
d (Å)	2.61	2.60	2.56	2.56
D_e (eV)	-1.43	-1.36	-1.69	-1.75
V_c (cm^{-1})	344.59	374.57	462.25	490.40
g_{\parallel}	1.69	1.73	1.81	1.83
g_{\perp}	-0.15	0.02	0.28	0.36
Mg₅O₅				
d (Å)	2.60			
D_e (eV)	-1.66			
V_c (cm^{-1})	355.78			
g_{\parallel}	1.70			
g_{\perp}	-0.10			
Mg₉O₉				
d (Å)	2.59	2.58	2.61	2.62
D_e (eV)	-1.68	-1.60	-1.00	-0.93
V_c (cm^{-1})	485.24	521.18	543.95	555.96
g_{\parallel}	1.82	1.85	1.86	1.86
g_{\perp}	0.35	0.45	0.50	0.53

to the experimental value. Our best embedded cluster results give $g_{\parallel} = 1.85$ and $g_{\perp} = 0.48$. This is surprisingly close to experiment and to the much simpler electrostatic calculations. We note that we verified that the ${}^2\Delta$ state is the ground state at the equilibrium adsorption height in the embedded cluster calculations.

4. Spin-orbit coupling

The spin-orbit coupling constant of the ${}^2\Delta$ state of TiH in the gas phase is about 119 cm^{-1} when calculated at the full-valence CASSCF level in a aug-cc-pVTZ basis, using the full Breit-Pauli Hamiltonian as implemented in Molpro. In embedded cluster calculations at the same level of theory, with the TiH 5 Å above the surface, we get almost the same result. At the equilibrium height ($\approx 2.6 \text{ Å}$) for the Mg₉O₉ cluster (extended with point charges), we find the slightly smaller value of 116 cm^{-1} at the CASSCF level of theory. When we improve the description of the electron correlation by computing the spin-orbit coupling at the MRCI level, using the full-valence active space of the CASSCF calculation as reference space, we find that the gas phase value becomes quite a bit smaller 110.17 cm^{-1} compared with 119 cm^{-1} at the CASSCF level. In the embedded cluster calculations, we also find that the spin-orbit coupling is smaller at the MRCI

level, but only by about 2 cm^{-1} . The most likely explanation for this is that, because of the larger numbers of electrons and orbitals in the embedded cluster calculations, we cannot include all the orbitals located on TiH that we included in the gas phase calculation. Hence, our best estimate for the spin-orbit coupling constant at the equilibrium adsorption height is 107 cm^{-1} , about 3 cm^{-1} below the gas phase MRCI value. The results in the figures and tables were obtained using the gas phase value. If we use our best estimate for the spin-orbit coupling from our most accurate embedded cluster calculation, we find $g_{\parallel} = 1.87$ and $g_{\perp} = 0.56$, even closer to the experimental values.

5. Dynamic model

With TiH in the ${}^2\Delta$ state, the Ti atom is slightly positive and the H atom slightly negative. Since the TiH is on top of the negative O ion, the equilibrium position is vertical in the electrostatic approximation. Still, there is always zero-point energy resulting in angular motion. This motion lowers the symmetry, which makes *ab initio* calculations harder. More importantly, since the two electronic states are nearly degenerate, angular motion will give rise to strong, possibly singular, nonadiabatic coupling. In Sec. S9 in the Supplemental Material [30], we present an electrostatic model to construct diabatic electronic states that allow us to compute the coupled electronic-nuclear motion. The results of the static calculations at the vertical geometry suggest that the electrostatics capture much of the physics of the system. In Fig. 4(c), we plot the angular potential and the inclination angle-dependent probability densities. The main conclusion is that the zero-point motion only has a small effect on the g tensor.

As the potential is nearly cylindrically symmetric, the hindered rotations are only weakly affected by the fourfold symmetry of the underlying MgO (see Fig. S20 in the Supplemental Material [30]). We therefore considered the probability density ρ as a function of the polar angle θ for azimuthal angle $\varphi = 0^\circ$, where the latter is defined to be toward one of the surrounding Mg atoms (or one of its fourfold symmetric equivalents). The perturbed ${}^2\Delta$ state is defined by two electronic states correlating with the two components of the ${}^2\Delta$ state that are separated by an energy of $\sim 70 \text{ meV}$. This suggests that the step observed in STS (Fig. S3 in the Supplemental Material, [19,20,22,30]) around $\pm 90 \text{ mV}$ may represent orbital excitation. As these excitations show variations in the presence of a magnetic tip but weak changes in magnetic field, we attribute these excitations to orbital excitations linked through spin-orbit coupling.

The low-energy-hindered rotational modes of TiH are well described by a two-dimensional quantum oscillator [Fig. 4(c)]. The lowest rotational level is $\sim 35 \text{ meV}$ above the bottom of the potential well. This is rather large compared with the rotational constant of TiH of $674 \mu\text{eV}$. Considering the steep potential energy barrier and its near cylindrical symmetry, we can rule out a multiwell potential and any tunneling of hydrogen related to the dynamic Jahn-Teller effect. The classical turning point of the lowest level at $\approx 15^\circ$ from the azimuth reflects the magnitude of the zero-point motion and the delocalization of the hydrogen wavefunction. We note that

the g tensor is insensitive to small perturbations of the internal Ti-H bond length [$\Delta g \approx 0.005$ for $\Delta R = 2$ pm, see Fig. 4(b) inset]. The potential resembles an anharmonic quantum oscillator, which is also signified by the uneven energy spacing of the low-lying states. As the excitation of the quantum oscillation and the orbital excitation will lead to a spatial variance of hydrogen, this most likely will lead to fluctuations of the spin polarization measured directly above the molecule with the STM probe. These points may need to be considered in measurements of the coherent properties of TiH on MgO based on pulsed ESR [24], which hitherto was reduced to a two-state system.

III. CONCLUSIONS

In conclusion, utilizing a millikelvin ESR-STM together with quantum modeling, based on QC and DFT, we quantified the interplay between the fine structure, geometry, and hindered rotations of an individual TiH molecule with unprecedented precision. Our measurements are exemplified by the striking observation of a giant anisotropy in the g tensor concurrent with a doublet ground state. Adopting QC calculations to account for electron correlation within the molecule and the effect of the surface, we demonstrated that the electronic ground state of TiH is modified near the surface and that this electronic ground state hosts a sizeable orbital angular momentum. TiH at the surface of MgO provides a clear example of a system, which cannot qualitatively or quantitatively be described by mean-field approaches and where correlation effects play a crucial role. Our calculations show that DFT strongly overestimates the splitting of the d states compared with the QC calculations. This finding is relevant in understanding the ESR mechanism for the TiH molecule [31]. From detailed embedded cluster calculations, we reproduced the observed anisotropic g tensor, which is highly sensitive to the height of the molecule above the surface. With this model, we also quantified the hindered rotational modes of the molecule and the orbital excitations of the molecule on the surface, which exhibit signatures like previous experimental observations. The combination of experiment and theory here provides an extremely powerful method to map out the fine structure of the molecule and relates it to the molecular geometry, going beyond what conventional SPM methods can provide. Moreover, the development of QC calculations for these classes of experiments provides a more accurate way of handling the electronic behavior and correlations of small molecules on surfaces as well as their resultant structural dynamics. In future experiments, it will be interesting to probe how the g tensor is modified by varying the adsorption site (e.g., bridge site) as well as by varying the insulator. Likewise, there are many questions raised concerning the ESR mechanism, utilizing a stable magnetic probe, such as the role of a noncollinear magnetization and spin pumping in the measured signal. In parallel, the observation of low frequency bands with millikelvin ESR-STM signal demonstrates the exquisite energy resolution of millikelvin-based STM. This development opens possibilities to explore spin coherence in quantum states of matter, as well as the response of superconducting materials to RF fields [42,43].

ACKNOWLEDGMENTS

We acknowledge funding from the Dutch Research Council (NWO), and the Vidi Project ‘‘Manipulating the interplay between superconductivity and chiral magnetism at the single-atom level’’ with Project No. 680-47-534. This project has received funding from the European Research Council (ERC) under the European Union’s Horizon 2020 research and innovation program (SPINAPSE: Grant Agreement No. 818399). F.D.N. thanks the Swiss National Science Foundation for financial support under Grant No. PP00P2_176866. The work of D.I.B., A.N.R. and V.V.M. was supported by Act 211 Government of the Russian Federation Contract No. 02.A03.21.0006.

M.S., W.M.J.v.W., and E.F.W. contributed equally to this paper.

APPENDIX A: MATERIALS AND METHODS

1. Experimental setup

Experiments were performed in a home-built ultra-high vacuum (UHV)-STM system, which was upgraded for ESR measurements [33]. If not stated otherwise, the base temperature for all experiments was $30 \text{ mK} \leq T_{\text{base}} \leq 55 \text{ mK}$. The system houses a vector magnetic field with maximal out-of-plane value of 9 T and a maximal in-plane value of 4 T. The field was swept while the STM tip was in tunneling contact. The in-plane magnetic field direction was oriented 23.8° with respect to the oxygen rows of the MgO surface. Electrochemically etched Cr bulk tips with a diameter of 0.5 mm were used. Tips were *in situ* cleaned by field emission before experiments. Additional Fe atoms were picked up to enhance spin-contrast.

The direct current (dc) bias voltage V_{DC} was applied to the tip, and the sample was virtually grounded, unlike in previous publications, e.g., Ref. [32], where V_{DC} was applied to the sample. STS (dI/dV) was recorded via a lock-in technique with the feedback loop opened after applying stabilization parameters V_{DC} and tunneling current I_t . A modulation voltage V_{mod} root mean square (RMS) was added to V_{DC} with modulation frequency $f_{\text{mod}} = 809 \text{ Hz}$. For the ESR experiments, a RF voltage was generated with an analog microwave signal generator (Keysight N5183B) and added to V_{DC} with a bias-tee at frequencies f_{RF} ranging from megahertz to gigahertz. Here, \tilde{P}_{RF} and \tilde{V}_{RF} denote the output power or voltage at the generator, and V_{RF} represents the RF voltage at the junction. Also, V_{RF} is given as the zero-to-peak value throughout this paper. To measure a current-signal compatible with the bandwidth of the preamplifier ($\approx 1 \text{ kHz}$), we used a well-established chopping scheme (15) at $f_{\text{chop}} = 877 \text{ Hz}$. The difference of the spin-polarized current ΔI_{ESR} is measured with a lock-in amplifier to optimize the signal-to-noise ratio.

2. Sample preparation

Samples were prepared *in situ* with a base pressure of $p \approx 10^{-10}$ mbar. Ag(100) was cleaned by repeated cycles of Ar⁺ sputtering ($p_{\text{Ar}} \approx 2 \times 10^{-5}$ mbar, $V_{\text{HV}} = 1.5 \text{ kV}$) and annealing ($T \approx 570^\circ \text{C}$). MgO was grown on Ag(100) by depositing

Mg from an effusion cell at $T_{\text{sample}} \approx 380^\circ\text{C}$ for 5 min in an oxygen atmosphere of $p_{\text{O}_2} \approx 3 \times 10^{-7}$ mbar. Fe and Ti atoms were codeposited onto the cold surface (<80 K) after MgO preparation.

APPENDIX B: EMBEDDED CLUSTER CALCULATIONS

We compute the g factors for TiH interacting with embedded clusters of four different sizes. The smallest cluster MgO consists of the O ion to which the TiH is attached and the Mg ion right below it. The second cluster Mg_5O has four additional Mg ions, which are the four xy plane nearest neighbors of the central O ion. The third cluster Mg_5O_5 also includes O ions below these four additional Mg ions. The largest cluster Mg_9O_9 consists of $3 \times 3 \times 2$ ions, i.e., it has four additional O ions on the surface, with Mg ions below them. In all cases, the central O ion is moved up by 0.48 \AA , and the Mg ion just below is moved down by 0.2 \AA compared with the other ions in the second layer. All these clusters were extended with $(2+, 2-)$ point charges to create a $21 \times 21 \times 2$ cluster. The TiH is perpendicular to the surface in these calculations, and the TiH bond distance is taken to be 1.773 \AA . The distance of the center of mass of TiH to the top layer of the crystal (d) was varied from 2.38 to 5.29 \AA (on a grid with steps of $0.1 a_0$ between 4.5 and $5.5 a_0$ and additional points at $d = 5.75, 6, 6.5, 7, 8, 9,$ and $10 a_0$).

All calculations were done with the Molpro 2015 QC program [40]. Molecular orbitals were calculated at the CASSCF level, with either the cc-pVDZ or cc-pVTZ correlation-consistent polarized-valence one-electron basis sets of double-zeta or triple-zeta quality. The calculations were done in C_{2v} point group symmetry. In all calculations, the active space consists of seven molecular orbitals and contains five electrons, corresponding to the valence orbitals and elec-

trons of TiH. In C_{2v} symmetry, this gives four orbitals of A_1 symmetry and an additional orbital in each of the remaining irreps ($B_1, B_2,$ and A_2), which we denote as $[4,1,1,1]$. The two electronic states correlating with the two components of the ${}^2\Delta$ state have symmetries A_1 and A_2 . We note that, if the LATTICE keyword of Molpro 2015 is used to add point charges, it is not possible to use symmetry. However, with the MATROP matrix operation facility of Molpro, it is possible to add Coulomb operators to the one-electron Hamiltonian, while still using symmetry.

To generate the initial orbital guess, we first calculated the molecular orbitals of the crystal and those of TiH separately. The TiH orbitals were calculated using the LQUANT,2 option of the CASSCF program to effectively use $C_{\infty v}$ symmetry and force $\Lambda = 2$, i.e., select the ${}^2\Delta$ state. The Molpro MERGE option was used to generate the orbital guess of the cluster by combining molecular orbitals of TiH with molecular orbitals of the cluster. The initial guess of the molecular orbitals of the crystal was obtained by merging orbitals of the O^{2-} and Mg^{2+} sublattices. This somewhat elaborate procedure guarantees convergence to the proper states and avoids artificial symmetry breaking and other convergence issues.

To investigate the effect of dynamic correlation, we performed internally contracted MRCI calculations with single and double excitations. The active space of the CASSCF calculations was used as reference space. A total of 13 electrons were correlated, with single and double excitations from four core orbitals, two A_1 , one B_1 , and one of B_2 symmetry. The effect of higher excitations was estimated with the Pople size-consistency correction (MRCI + Q).

The computation of the g factors requires matrix elements of the orbital angular momentum operator \hat{L}_z between the two electronic states correlating with the ${}^2\Delta$ state and also the spin-orbit interaction between these states.

-
- [1] J. Repp, G. Meyer, S. M. Stojković, A. Gourdon, and C. Joachim, Molecules on Insulating Films: Scanning-tunneling Microscopy Imaging of Individual Molecular Orbitals, *Phys. Rev. Lett.* **94**, 026803 (2005).
- [2] L. Gross, F. Mohn, N. Moll, P. Liljeroth, and G. Meyer, The chemical structure of a molecule resolved by atomic force microscopy, *Science* **325**, 1110 (2009).
- [3] A. Wachowiak, R. Yamachika, K. H. Khoo, Y. Wang, M. Grobis, D. H. Lee, S. G. Louie, and M. F. Crommie, Visualization of the molecular Jahn-Teller effect in an insulating K_4C_{60} monolayer, *Science* **310**, 468 (2005).
- [4] X. H. Qiu, G. V. Nazin, and W. Ho, Vibrationally resolved fluorescence excited with submolecular precision, *Science* **299**, 542 (2003).
- [5] B. C. Stipe, M. A. Rezaei, and W. Ho, Single-molecule vibrational spectroscopy and microscopy, *Science* **280**, 1732 (1998).
- [6] S. Li, A. Yu, F. Toledo, Z. Han, H. Wang, H. Y. He, R. Wu, and W. Ho, Rotational and Vibrational Excitations of a Hydrogen Molecule Trapped within a Nanocavity of Tunable Dimension, *Phys. Rev. Lett.* **111**, 146102 (2013).
- [7] F. D. Natterer, F. Patthey, and H. Brune, Distinction of Nuclear Spin States with the Scanning Tunneling Microscope, *Phys. Rev. Lett.* **111**, 175303 (2013).
- [8] L. J. Lauhon and W. Ho, Single-molecule vibrational spectroscopy and microscopy: CO on Cu(001) and Cu(110), *Phys. Rev. B* **60**, R8525 (1999).
- [9] P. P. Borbat, H. S. McHaourab, and J. H. Freed, Protein structure determination using long-distance constraints from double-quantum coherence ESR: Study of T4 lysozyme, *J. Am. Chem. Soc.* **124**, 5304 (2002).
- [10] E. J. Hustedt, A. I. Smirnov, C. F. Laub, C. E. Cobb, and A. H. Beth, Molecular distances from dipolar coupled spin-labels: The global analysis of multifrequency continuous wave electron paramagnetic resonance data, *Biophys. J.* **72**, 1861 (1997).
- [11] N. Hauptmann, M. Dupé, T.-C. Hung, A. K. Lemmens, D. Wegner, B. Dupé, and A. A. Khajetoorians, Revealing the correlation between real-space structure and chiral magnetic order at the atomic scale, *Phys. Rev. B* **97**, 100401(R) (2018).
- [12] M. Emmrich, F. Huber, F. Pielmeier, J. Welker, T. Hofmann, M. Schneiderbauer, D. Meuer, S. Polesya, S. Mankovsky, D. Ködderitzsch, H. Ebert, and F. J. Giessibl, Subatomic resolution force microscopy reveals internal structure and adsorption sites of small iron clusters, *Science* **348**, 308 (2015).
- [13] S. Loth, M. Etzkorn, C. P. Lutz, D. M. Eigler, and A. J. Heinrich, Measurement of fast electron spin relaxation times with atomic resolution, *Science* **329**, 1628 (2010).

- [14] G. Nunes and M. R. Freeman, Picosecond resolution in scanning tunneling microscopy, *Science* **262**, 1029 (1993).
- [15] S. Baumann, W. Paul, T. Choi, C. P. Lutz, A. Ardavan, and A. J. Heinrich, Electron paramagnetic resonance of individual atoms on a surface, *Science* **350**, 417 (2015).
- [16] T. L. Cocker, V. Jelic, M. Gupta, S. J. Molesky, J. A. J. Burgess, G. D. L. Reyes, L. V. Titova, Y. Y. Tsui, M. R. Freeman, and F. A. Hegmann, An ultrafast terahertz scanning tunnelling microscope, *Nat. Photonics* **7**, 620 (2013).
- [17] M. Garg and K. Kern, Attosecond coherent manipulation of electrons in tunneling microscopy, *Science* **367**, 411 (2020).
- [18] T. L. Cocker, D. Peller, P. Yu, J. Repp, and R. Huber, Tracking the ultrafast motion of a single molecule by femtosecond orbital imaging, *Nature* **539**, 263 (2016).
- [19] F. D. Natterer, F. Patthey, T. Bilgeri, P. R. Forrester, N. Weiss, and H. Brune, Upgrade of a low-temperature scanning tunneling microscope for electron-spin resonance, *Rev. Sci. Instrum.* **90**, 013706 (2019).
- [20] T. S. Seifert, S. Kovarik, C. Nistor, L. Persichetti, S. Stepanow, and P. Gambardella, Single-atom electron paramagnetic resonance in a scanning tunneling microscope driven by a radio-frequency antenna at 4 K, *Phys. Rev. Research* **2**, 013032 (2020).
- [21] F. Meier, L. Zhou, J. Wiebe, and R. Wiesendanger, Revealing magnetic interactions from single-atom magnetization curves, *Science* **320**, 82 (2008).
- [22] K. Yang, Y. Bae, W. Paul, F. D. Natterer, P. Willke, J. L. Lado, A. Ferrón, T. Choi, J. Fernández-Rossier, A. J. Heinrich, and C. P. Lutz, Engineering the Eigenstates of Coupled Spin-1/2 Atoms on a Surface, *Phys. Rev. Lett.* **119**, 227206 (2017).
- [23] P. Willke, Y. Bae, K. Yang, J. L. Lado, A. Ferrón, T. Choi, A. Ardavan, J. Fernández-Rossier, A. J. Heinrich, and C. P. Lutz, Hyperfine interaction of individual atoms on a surface, *Science* **362**, 336 (2018).
- [24] K. Yang, W. Paul, S. H. Phark, P. Willke, Y. Bae, T. Choi, T. Esat, A. Ardavan, A. J. Heinrich, and C. P. Lutz, Coherent spin manipulation of individual atoms on a surface, *Science* **366**, 509 (2019).
- [25] A. Burrows, M. Dulick, C. W. Bauschlicher, P. F. Bernath, R. S. Ram, C. M. Sharp, and J. A. Milsom, Spectroscopic constants, abundances, and opacities of the TiH molecule, *Astrophys. J.* **624**, 988 (2005).
- [26] V. I. Anisimov, J. Zaanen, and O. K. Andersen, Band theory and mott insulators: Hubbard u instead of Stoner I , *Phys. Rev. B* **44**, 943 (1991).
- [27] A. Georges, G. Kotliar, W. Krauth, and M. J. Rozenberg, Dynamical mean-field theory of strongly correlated fermion systems and the limit of infinite dimensions, *Rev. Mod. Phys.* **68**, 13 (1996).
- [28] S. Schintke, S. Messerli, M. Pivetta, F. Patthey, L. Libioulle, M. Stengel, A. De Vita, and W. D. Schneider, Insulator at the Ultrathin Limit: MgO on Ag(001), *Phys. Rev. Lett.* **87**, 276801 (2001).
- [29] G. Pacchioni and H. Freund, Electron transfer at oxide surfaces. The MgO paradigm: From defects to ultrathin films, *Chem. Rev.* **113**, 4035 (2013).
- [30] See Supplemental Material at <http://link.aps.org/supplemental/10.1103/PhysRevB.103.155405> for further details, including Secs. S1–S9, Figs. S1–S22, Tables S1–S5, and Refs. [44–64].
- [31] A. Ferrón, S. A. Rodríguez, S. S. Gómez, J. L. Lado, and J. Fernández-Rossier, Single spin resonance driven by electric modulation of the g -factor anisotropy, *Phys. Rev. Research* **1**, 033185 (2019).
- [32] H. von Allwörden, A. Eich, E. J. Knol, J. Hermenau, A. Sonntag, J. W. Gerritsen, D. Wegner, and A. A. Khajetoorians, Design and performance of an ultra-high vacuum spin-polarized scanning tunneling microscope operating at 30 mK and in a vector magnetic field, *Rev. Sci. Instrum.* **89**, 033902 (2018).
- [33] W. M. J. van Weerdenburg, M. Steinbrecher, N. P. E. van Mullekom, J. W. Gerritsen, H. von Allwörden, F. D. Natterer, and A. A. Khajetoorians, A scanning tunneling microscope capable of electron spin resonance and pump-probe spectroscopy at mK temperature and in vector magnetic field, *Rev. Sci. Instrum.* **92**, 033906 (2021).
- [34] U. Kamber, A. Bergman, A. Eich, D. Iuşan, M. Steinbrecher, N. Hauptmann, L. Nordström, M. I. Katsnelson, D. Wegner, O. Eriksson, and A. A. Khajetoorians, Self-induced spin glass state in elemental and crystalline neodymium, *Science* **368**, eaay6757 (2020).
- [35] A. M. Tselvelick and P. B. Wiegmann, Exact results in the theory of magnetic alloys, *Adv. Phys.* **32**, 453 (1983).
- [36] K. Yang, W. Paul, F. D. Natterer, J. L. Lado, Y. Bae, P. Willke, T. Choi, A. Ferrón, J. Fernández-Rossier, A. J. Heinrich, and C. P. Lutz, Tuning the Exchange Bias on a Single Atom from 1 mT to 10 T, *Phys. Rev. Lett.* **122**, 227203 (2019).
- [37] Y. Bae, K. Yang, P. Willke, T. Choi, A. J. Heinrich, and C. P. Lutz, Enhanced quantum coherence in exchange coupled spins via singlet-triplet transitions, *Sci. Adv.* **4**, eaau4159 (2018).
- [38] P. Willke, W. Paul, F. D. Natterer, K. Yang, Y. Bae, T. Choi, J. Fernández-Rossier, A. J. Heinrich, and C. P. Lutz, Probing quantum coherence in single-atom electron spin resonance, *Sci. Adv.* **4**, eaq1543 (2018).
- [39] T. S. Seifert, S. Kovarik, D. M. Juraschek, N. A. Spaldin, P. Gambardella, and S. Stepanow, Longitudinal and transverse electron paramagnetic resonance in a scanning tunneling microscope, *Sci. Adv.* **6**, eabc5511 (2020).
- [40] H. J. Werner, P. J. Knowles, G. Knizia, F. R. Manby, and M. Schütz, Molpro: A package of *ab initio* programs, version 2015.1, <http://www.molpro.net> (version 2015).
- [41] J. E. Lennard-Jones and B. M. Dent, Cohesion at a crystal surface, *Trans. Faraday Soc.* **24**, 92 (1928).
- [42] P. Kot, R. Drost, M. Uhl, J. Ankerhold, J. C. Cuevas, and C. R. Ast, Microwave-assisted tunneling and interference effects in superconducting junctions under fast driving signals, *Phys. Rev. B* **101**, 134507 (2020).
- [43] O. Peters, N. Bogdanoff, S. Acero González, L. Melischek, J. R. Simon, G. Reecht, C. B. Winkelmann, F. von Oppen, and K. J. Franke, Resonant Andreev reflections probed by photon-assisted tunnelling at the atomic scale, *Nat. Phys.* **16**, 1222 (2020).
- [44] W. Paul, K. Yang, S. Baumann, N. Romming, T. Choi, C. P. Lutz, and A. J. Heinrich, Control of the millisecond spin lifetime of an electrically probed atom, *Nat. Phys.* **13**, 403 (2016).
- [45] W. Paul, S. Baumann, C. P. Lutz, and A. J. Heinrich, Generation of constant-amplitude radio-frequency sweeps at a tunnel junction for spin resonance STM, *Rev. Sci. Instrum.* **87**, 074703 (2016).

- [46] A. A. Khajetoorians, B. Chilian, J. Wiebe, S. Schuwalow, F. Lechermann, and R. Wiesendanger, Detecting excitation and magnetization of individual dopants in a semiconductor, *Nature* **467**, 1084 (2010).
- [47] A. A. Khajetoorians, B. Baxevis, C. Hübner, T. Schlenk, S. Krause, T. O. Wehling, S. Lounis, A. Lichtenstein, D. Pfannkuche, J. Wiebe, and R. Wiesendanger, Current-driven spin dynamics of artificially constructed quantum magnets, *Science* **339**, 55 (2013).
- [48] L. Zhou, J. Wiebe, S. Lounis, E. Vedmedenko, F. Meier, S. Blügel, P. H. Dederichs, and R. Wiesendanger, Strength and directionality of surface Ruderman-Kittel-Kasuya-Yosida interaction mapped on the atomic scale, *Nat. Phys.* **6**, 187 (2010).
- [49] A. A. Khajetoorians, S. Lounis, B. Chilian, A. T. Costa, L. Zhou, D. L. Mills, J. Wiebe, and R. Wiesendanger, Itinerant Nature of Atom-Magnetization Excitation by Tunneling Electrons, *Phys. Rev. Lett.* **106**, 037205 (2011).
- [50] A. A. Khajetoorians, J. Wiebe, B. Chilian, S. Lounis, S. Blügel, and R. Wiesendanger, Atom-by-atom engineering and magnetometry of tailored nanomagnets, *Nat. Phys.* **8**, 497 (2012).
- [51] S. Baumann, F. Donati, S. Stepanow, S. Rusponi, W. Paul, S. Gangopadhyay, I. G. Rau, G. E. Pacchioni, L. Gragnaniello, M. Pivetta, J. Dreiser, C. Piamonteze, C. P. Lutz, R. M. Macfarlane, B. A. Jones, P. Gambardella, A. J. Heinrich, and H. Brune, Origin of Perpendicular Magnetic Anisotropy and Large Orbital Moment in Fe Atoms on MgO, *Phys. Rev. Lett.* **115**, 237202 (2015).
- [52] J. P. Perdew, K. Burke, and M. Ernzerhof, Generalized Gradient Approximation Made Simple, *Phys. Rev. Lett.* **77**, 3865 (1996).
- [53] G. Kresse and J. Furthmüller, Efficient iterative schemes for *ab initio* total-energy calculations using a plane-wave basis set, *Phys. Rev. B* **54**, 11169 (1996).
- [54] A. I. Liechtenstein, V. I. Anisimov, and J. Zaanen, Density-functional theory and strong interactions: Orbital ordering in Mott-Hubbard insulators, *Phys. Rev. B* **52**, R5467 (1995).
- [55] J. T. Hougen and G. G. Wiersma, *The Calculation of Rotational Energy Levels and Rotational Line Intensities in Diatomic Molecules* (National Bureau of Standards, Washington, D.C., 1970), Vol. 115.
- [56] G. Dhont, W. B. Zeimen, G. C. Groenenboom, and A. van der Avoird, Theoretical study of the He-HF⁺ complex. II. Rovibronic states from coupled diabatic potential energy surfaces, *J. Chem. Phys.* **120**, 103 (2004).
- [57] T. H. Dunning, Gaussian basis sets for use in correlated molecular calculations. I. The atoms boron through neon and hydrogen, *J. Chem. Phys.* **90**, 1007 (1989).
- [58] H. J. Werner and P. J. Knowles, A second order multiconfiguration SCF procedure with optimum convergence, *J. Chem. Phys.* **82**, 5053 (1985).
- [59] P. J. Knowles and H.-J. Werner, An efficient second-order MC SCF method for long configuration expansions, *Chem. Phys. Lett.* **115**, 259 (1985).
- [60] H. J. Werner and P. J. Knowles, An efficient internally contracted multiconfiguration-reference configuration interaction method, *J. Chem. Phys.* **89**, 5803 (1988).
- [61] P. J. Knowles and H.-J. Werner, An efficient method for the evaluation of coupling coefficients in configuration interaction calculations, *Chem. Phys. Lett.* **145**, 514 (1988).
- [62] K. R. Shamasundar, G. Knizia, and H. J. Werner, A new internally contracted multi-reference configuration interaction method, *J. Chem. Phys.* **135**, 054101 (2011).
- [63] G. Schaftenaar and J. H. Noordik, Molden: A pre- and post-processing program for molecular and electronic structures, *J. Comput. Aided Mol. Des.* **14**, 123 (2000).
- [64] G. Schaftenaar, E. Vlieg, and G. Vriend, Molden 2.0: Quantum chemistry meets proteins, *J. Comput. Aided Mol. Des.* **31**, 789 (2017).